

# Towards Hourly 4-D Subsurface Monitoring using Seismic Ambient Noise

Peng Guo<sup>1,\*</sup> and Erdinc Saygin<sup>1,2</sup>

<sup>1</sup> Deep Earth Imaging Future Science Platform, The Commonwealth Scientific and Industrial Research Organisation (CSIRO), Kensington 6151, Western Australia, Australia.

<sup>2</sup> Department of Physics, School of Physics, Mathematics and Computing, Faculty of Engineering and Mathematical Sciences, University of Western Australia, Crawley 6009, Western Australia, Australia.

Corresponding author: Peng Guo ([peng.guo@csiro.au](mailto:peng.guo@csiro.au))

## Key Points:

- We present a new method for high-resolution 4-D passive monitoring of subsurface physical property.
- We compute hourly quantitative time-lapse images of velocity changes in the horizontal and depth domain from offshore ambient noise.
- The method opens new avenues for 4-D monitoring using ambient noise from dense arrays and DAS.

## 21 **Abstract**

22 We use seismic ambient noise recorded by the ocean bottom nodes (OBNs) in the Gorgon gas  
23 field, Western Australia to compute time-lapse seafloor models. The extracted hourly cross-  
24 correlation (CC) functions of 0.1 – 1 Hz contain mainly Scholte waves with very high signal to  
25 noise ratio. The conventional time-lapse analysis suggests relative velocity variations ( $dv/v$ ) up  
26 to 1% assuming a spatially homogeneous  $dv/v$ , with a likely 24-hour cycling pattern. With high-  
27 resolution baseline models from full waveform inversion of Scholte waves, we propose a double-  
28 difference waveform inversion (DD-WI) method using travel time differences for localizing the  
29 time-lapse  $dv/v$  in the heterogeneous subsurface in depth. The time-lapse velocity models show  
30 velocity increase/decrease patterns in agreement with that from conventional analysis, with more  
31 notable changes at the shallower depths. We demonstrate the feasibility of using ambient noise  
32 for quantitative monitoring of subsurface property changes in the horizontal and depth domain at  
33 an hourly basis.

## 34 **1 Introduction**

35 Temporal variations of subsurface physical properties have been commonly observed, for  
36 example, within active volcanos and fault zones, natural resources (e.g., hydrocarbon,  
37 geothermal) production fields, and carbon/hydrogen capture/storage in rock reservoirs (Lumley,  
38 2001; Brenguier et al., 2008; Takano et al., 2014; Roche et al., 2021). Seismic monitoring using  
39 environmental ambient noise (passive seismic data) has been demonstrated as a powerful and  
40 cost-effective solution for detecting and quantifying such property changes (Sens-Schönfelder  
41 and Wegler, 2006). A simple cross-correlation (CC) of ambient noise wavefield recorded at two  
42 receivers reconstructs the virtual interstation Green's function, which can be interpreted as the  
43 seismic response that would be measured at one of the receiver locations as if there is a source at  
44 the other location (e.g., Shapiro and Campillo, 2004). The ever-present natural ambient sources  
45 enable continuous and reliable retrievals of the seismic responses between pairs of stations  
46 across times, for example at a daily (de Ridder and Biondi, 2013) or hourly basis (Mao et al.,  
47 2019); the waveform changes (e.g., the travel time shifts) from the time-lapse CC functions can  
48 be used for deriving the temporal variations of seismic velocity ( $dv/v$ ) (Richter et al., 2014).  
49 Compared with expensive controlled-source seismic survey for time-lapse monitoring (Hicks et  
50 al., 2016), seismic monitoring using ambient noise helps reduce the operational cost significantly

51 and is also environmentally friendly; it is also preferred to monitoring methods using nature-  
52 sourced earthquakes because of the lack of repeatability and universal distribution for the latter  
53 (Kamei and Lumley, 2017).

54 Previous studies suggest that seismic ambient noise is mainly originated from the interaction of  
55 the ocean with the solid earth (Stehly et al., 2006; Gualtieri et al., 2020). The main signals  
56 extracted from seismic ambient noise are usually surface waves (e.g., Shapiro and Campillo,  
57 2004; Stehly et al., 2006; Brenguier et al., 2016), albeit body waves have also been observed  
58 (e.g., Roux et al., 2005; Nakata et al., 2016; Saygin et al., 2017). Both the coda part and direct  
59 (ballistic) arrivals of the extracted seismic responses have been used for monitoring and can be  
60 sensitive to minor velocity changes at the order of 0.1% (Sens-Schönfelder and Wegler, 2006;  
61 Brenguier et al., 2020; Takano et al., 2020). It is of common practice for seismic passive  
62 monitoring to detect the temporal changes with a spatially homogeneous change assumption  
63 (Sens-Schönfelder and Wegler, 2006), however it remains challenging to characterize their  
64 detailed spatial distribution. There have been studies using ballistic surface wave arrivals (de  
65 Ridder and Biondi, 2013; de Ridder et al., 2014; Mordret et al., 2014) that localize the velocity  
66 changes in the horizontal plane but without determining the depth extent, and using the eikonal  
67 equation for describing the physics which is less accurate than inversion methods based on the  
68 elastic-wave equation. Mordret et al. (2020) estimate velocity changes in depth from dispersion  
69 measurements however with a 1-D assumption. The spatial extent of changes has also been  
70 determined using coda sensitivity kernels (Obermann et al., 2013; Rodríguez Tribaldos et al.,  
71 2021) but the resolution is relatively low. Compared with the established workflows for  
72 determining quantitative 4-D (space-time) models of temporal velocity changes using body  
73 waves from controlled seismic sources (e.g., Lumley, 2001; Zhang & Huang, 2013; Yang et al.,  
74 2016; Hicks et al., 2016), there has been a significant knowledge gap for subsurface real-time  
75 monitoring using surface waves from ambient noise.

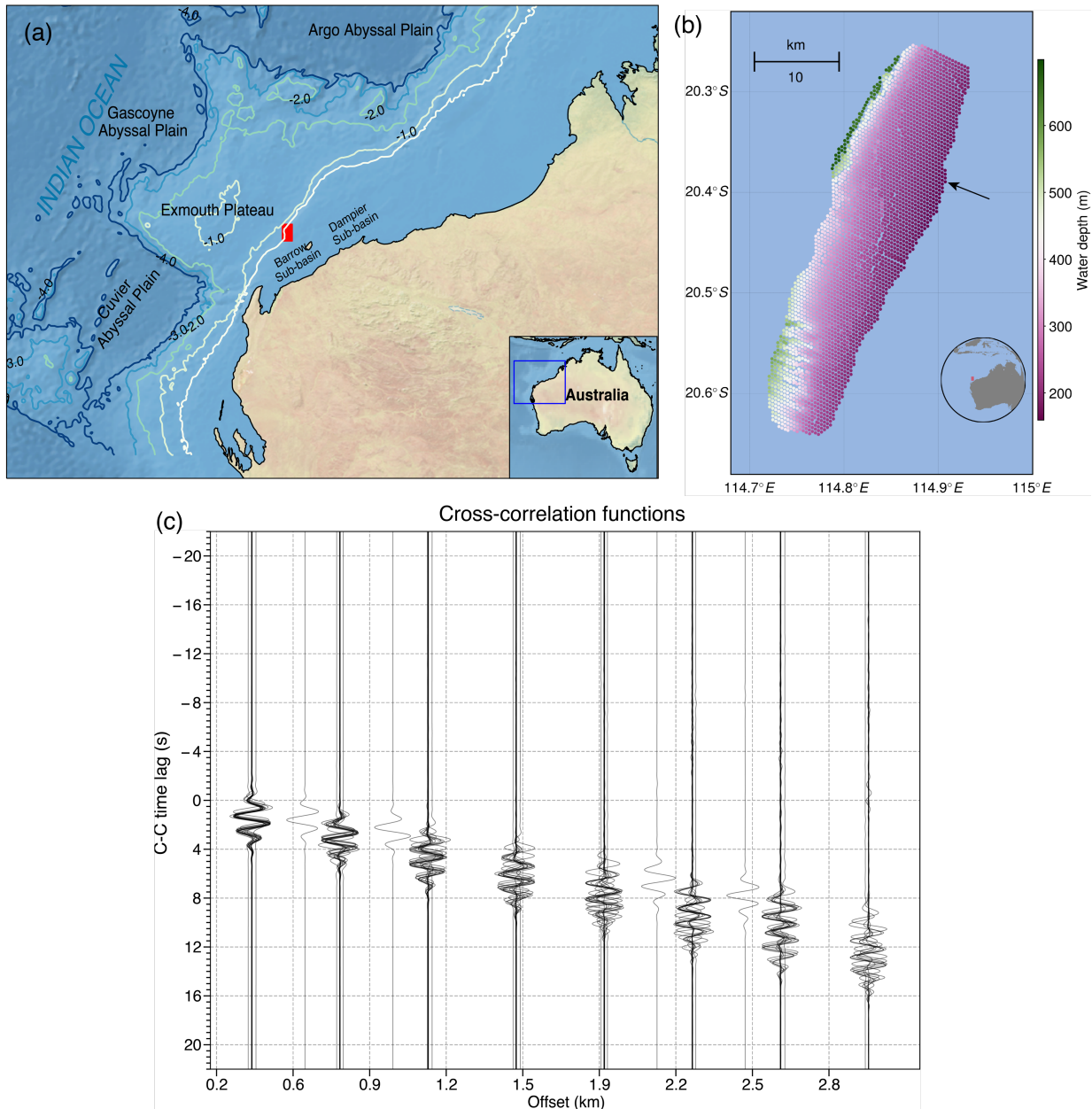
76 Seismic monitoring using ambient noise has great potential for industrial applications, including  
77 the real-time monitoring of carbon/hydrogen geological storage in subsurface rock reservoirs for  
78 the ongoing decarbonization efforts. We present a study for spatio-temporal monitoring of the  
79 subsurface heterogeneous physical property changes using offshore seismic ambient noise. We  
80 extract hourly Scholte wave of 0.1 – 1 Hz from two-day seafloor seismic noise recorded by the

81 vertical component of ocean bottom nodes (OBNs). Time-lapse analysis shows temporal changes  
82 of the seafloor velocity ( $dv/v$ ) up to  $\sim 1\%$ . With a baseline seafloor model from FWI of Scholte  
83 waves, we propose a double-difference waveform inversion (DD-WI) method using differential  
84 arrival times for estimating high-resolution time-lapse velocity models. Synthetic and field data  
85 studies show that it is feasible for 4-D real-time quantitative monitoring using ambient noise, i.e.,  
86 detecting and localizing subtle subsurface velocity changes in the horizontal and depth domain at  
87 an hourly basis using ambient noise data from dense arrays.

## 88 **2 Data and ambient noise interferometry**

89 Between 2015 and 2016, Chevron Australia and its partners acquired a 3-D OBN seismic survey  
90 over the Gorgon gas field for a better description of the Gorgon reservoir sands for carbon  
91 capture and storage, with the survey area located in the North West Shelf offshore of Western  
92 Australia, approximately 200 km from the mainland (Fig. 1a and 1b). Both the in-line and cross-  
93 line intervals were 375 m, with 120 OBN lines covering an area of  $\sim 436 \text{ km}^2$ . The inline  
94 direction was  $115^\circ/295^\circ$ , about perpendicular to the coastal line. The water depth in the survey  
95 region was between 200 - 600 m. Each node comprised four channels, with two horizontal  
96 components (X, Y) and one vertical component (Z) for measuring displacement, and a  
97 hydrophone component for recording pressure. The data were recorded continuously with a 2  
98 millisecond interval. The survey used controlled air-gun seismic sources, but there were several  
99 quiet time windows without using controlled active sources. The recorded ambient seismic  
100 wavefield in the absence of active seismic sources provides the opportunity for passive seismic  
101 monitoring using a dense seismic array of industrial scale. We select a time window of Julian  
102 Days 1 and 2 of 2016 for the passive seismic monitoring experiment.

Gorgon OBN Seismic Survey (2015-2016)



103

104 Fig. 1. Map of the ocean bottom seismic survey in Western Australia and cross-correlation (CC) functions from  
 105 ambient noise interferometry. (a) Ocean Bottom Node (OBN) seismic survey in the Gorgon gas field offshore  
 106 Western Australia by Chevron Australia and its partners. (b) Zoom-in of the red rectangle in (a), with the color on  
 107 the OBNs suggesting water depths; the black arrow indicates Line 3924. (c) CC functions for Line 3924 sorted by  
 108 offsets (the distance between stations of a station pair) from Hour 15 of Julian Day 1, 2016. We limit the CC  
 109 functions to 3 km.

110

We detrend and down-sample the vertical component of the data from 250 Hz to 20 Hz with  
 111 anti-aliasing filtering. The ambient noise data are then filtered at 0.1 – 1 Hz. We divide the

112 recordings of the selected quiet time window without active source shooting into hour-long  
113 segments; each segment is then subdivided into 30 s long records with a 50% overlap. Green's  
114 functions are reconstructed by computing CC functions of the 30 s ambient noise window  
115 between station pairs. We use weighted phase stacking (Schimmel et al., 2011) for stacking the  
116 CC functions within each hour-long segment to improve the signal to noise ratio. Fig. 1c shows  
117 the CC functions at Hour 15 Day 1 for Line 3924 (indicated by the black arrow in Fig. 1b),  
118 which contain mainly Scholte waves (travelling along the interface between the seawater and  
119 seafloor) and provide constraints for the shear-wave velocity of the seafloor. The hourly  
120 extracted CC functions have a very high signal to noise ratio. The energy concentrates on the  
121 positive side of the CC time lags, suggesting that the ambient noise between 0.1 and 1 Hz  
122 propagates from the ocean to the coast.

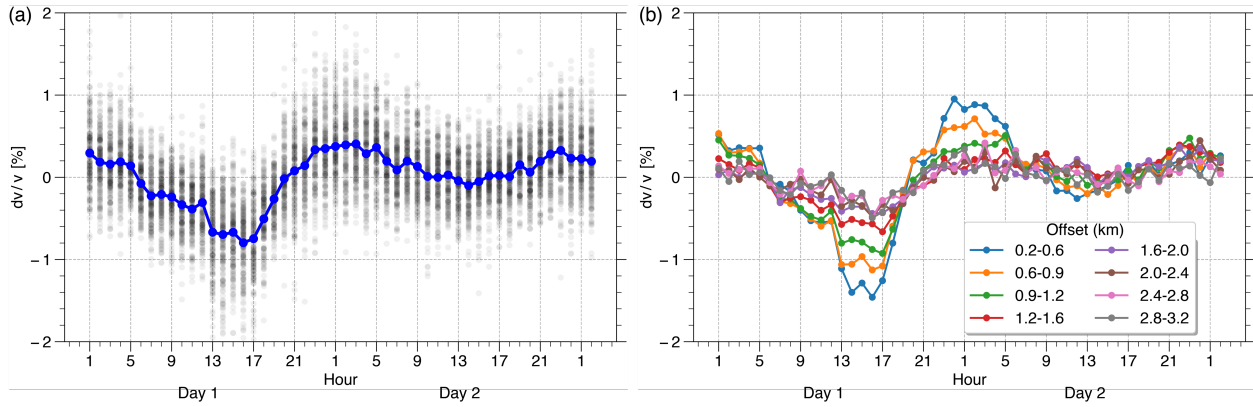
### 123 **3 Methods and results**

#### 124 **3.1 Seismic velocity temporal monitoring**

125 A baseline (reference) data for each station pair can be obtained by stacking the hourly CC  
126 functions across all the available hours from the two-day passive recordings. We compare the  
127 ballistic part of the Scholte wave arrivals of the baseline data with that of the hourly CC  
128 functions for quantifying the temporal velocity variations. The conventional time-lapse analysis  
129 using the stretching method assumes that the relative velocity variation ( $dv/v$ ) is uniform in  
130 space, therefore we have the relation of  $dv/v$  with the relative travel time change ( $dt/t$ ) as  
131  $dv/v = -dt/t$  (Sens-Schönfelder and Wegler, 2006). Fig. 2 shows the derived velocity changes  
132 across the two days. We notice that the seafloor velocity changes up to 1% (Fig. 2a), with a  
133 likely sinusoidal pattern of  $\sim 24$ -hour cycle. The smaller offsets, which provide constraints for  
134 the shallower depths, generally have larger velocity variations than those from the relatively  
135 larger offsets (Fig. 2b), which are more associated with the velocities at the greater depths. The  
136 velocity changes from Fig. 2 can be interpreted as the average velocity changes of the seafloor  
137 where the extracted Scholte waves propagate through. The temporal changes of velocities from

138 more survey lines, as indicated by the black arrows in Fig. S1, are shown in Fig. S2, which  
 139 suggests similar patterns of velocity temporal changes with Fig 2.

140

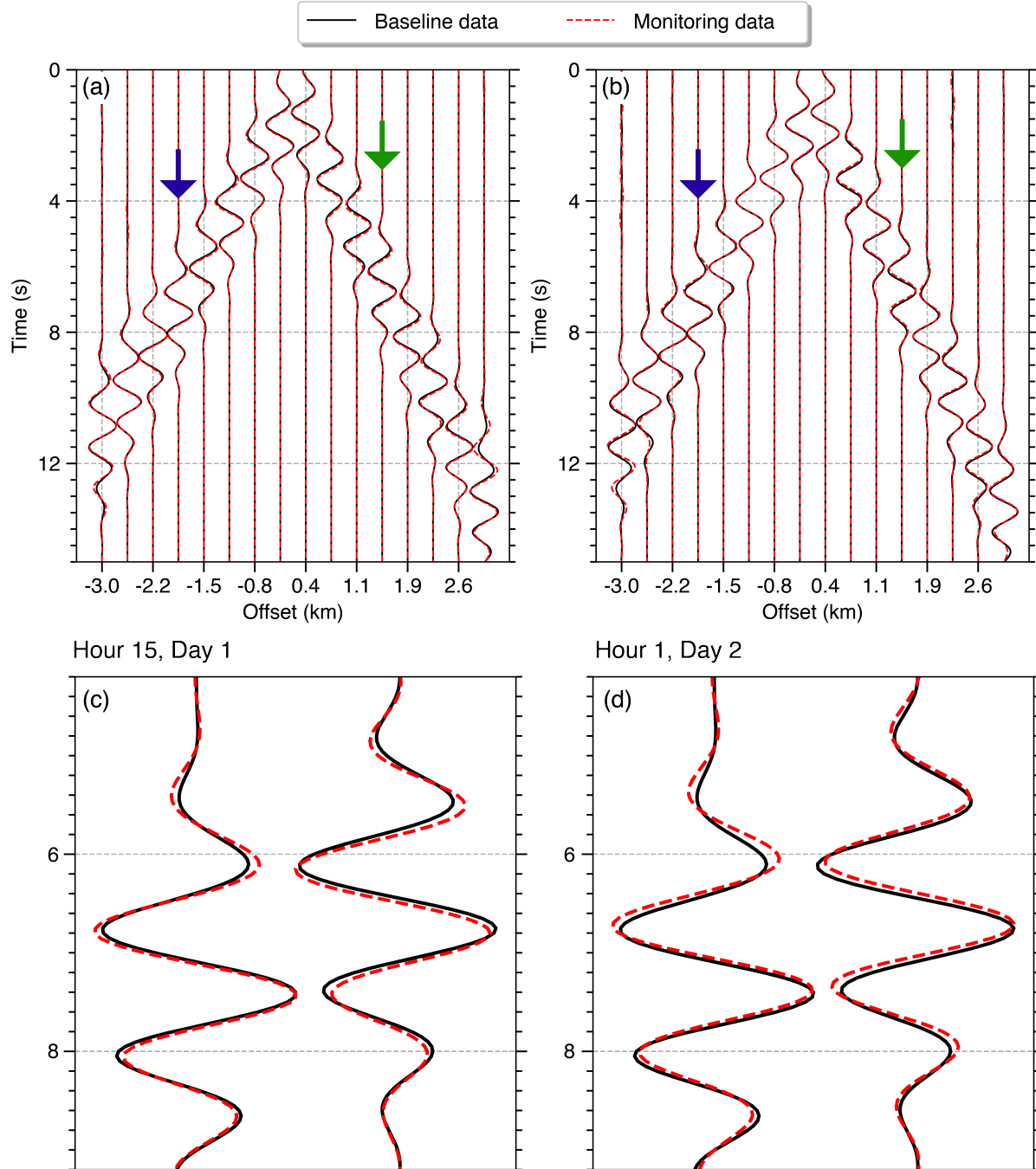


141

142 Fig. 2. The relative velocity temporal changes ( $dv/v$ ) from the stretching method. (a)  $dv/v$  of the seafloor  
 143 at an hourly basis for Julian Day 1 and Day 2 of 2016. The velocity changes were estimated from the  
 144 ballistic part of the extracted Scholte waves in Line 3924. Each black dot is the  $dv/v$  from a station pair  
 145 measurement. The blue curve is the average  $dv/v$ . (b) The average velocity changes from CC functions of  
 146 different offset ranges, for example ‘0.2-0.6’ refers to CC functions of 0.2 – 0.6 km offset.

147

148 We sort the CC functions of all the station pairs into common-station gathers. Each common-  
 149 station gather can be considered as a seismic common-source gather that the shared common  
 150 station is the source, and the rest of the stations from the selected survey line are the receivers. Fig.  
 151 3 contains common-station gathers of the baseline data and the monitoring data from Hour 15 of  
 152 Day 1 (Fig. 3a) and Hour 1 of Day 2 (Fig. 3b). We observe that the main difference between the  
 153 baseline and monitoring data of different hours are the arrival times of the Scholte waves. Scholte  
 154 waves from Hour 15 of Day 1 arrive later than the baseline data (Fig. 3a, 3c), indicating a velocity  
 155 decrease than the baseline model, while those from Hour 1 of Day 2 arrive at an earlier time than  
 156 the baseline data (Fig. 3b, 3d), suggesting a velocity increase; these observations from the  
 157 common-station gathers are consistent with Fig. 2.



158

159 Fig. 3. Common-station gathers sorted from CC functions of station pairs of Line 3924. (a) is the  
 160 comparison of the baseline data (solid black curve) and the monitoring data (dashed red curve) of Hour 15  
 161 Day 1. (b) is the comparison of the baseline data (solid black curve) and the monitoring data (dashed red  
 162 curve) of Hour 1 Day 2. (c) and (d) are zoom-in of the seismic trace at -1.9 km and 1.5 km offsets (from  
 163 left to right, indicated by the blue and green arrows, respectively) from (a) and (b).

164

### 165 **3.2 Full waveform inversion for baseline model estimation**

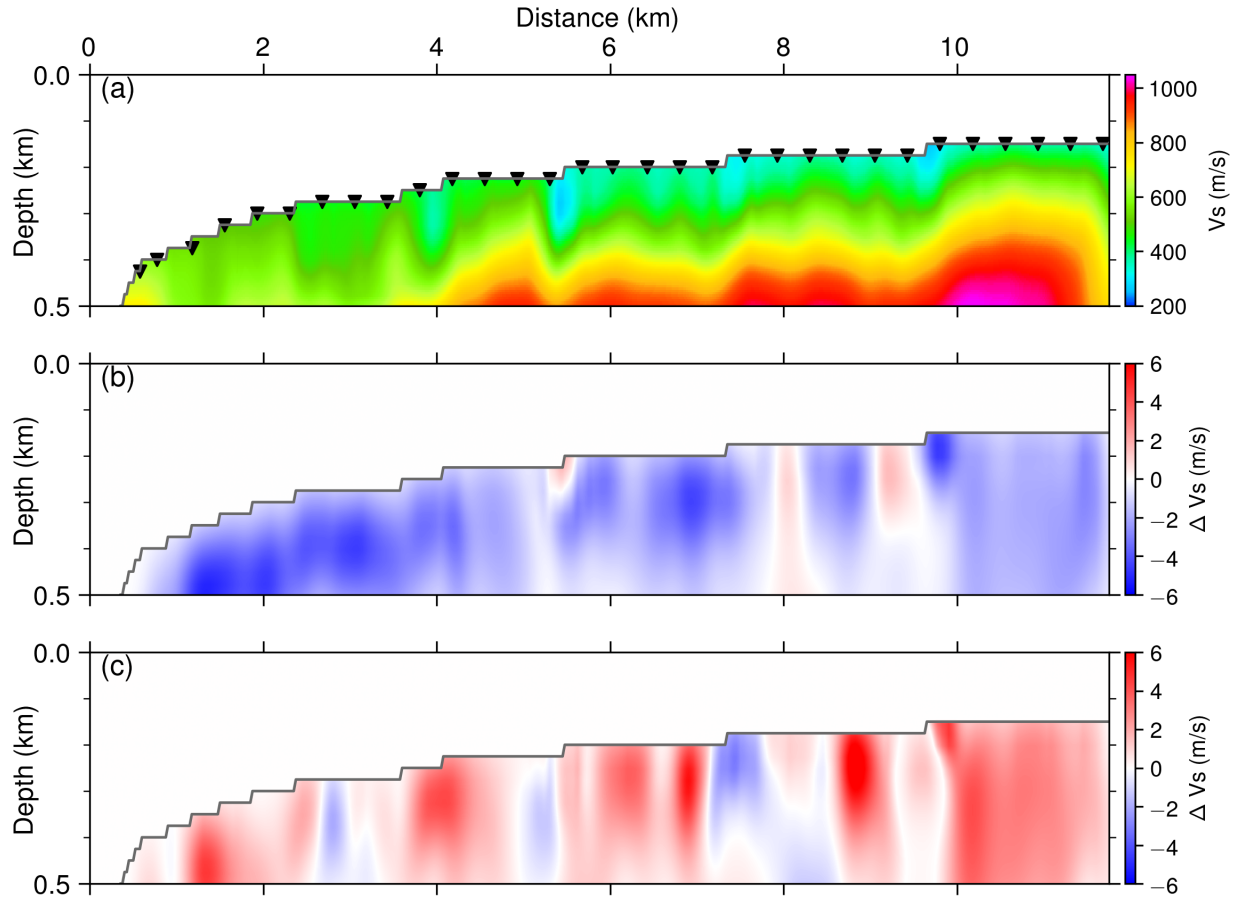
166 The dense array of OBNs provides the opportunity for computing time-lapse quantitative images  
167 of velocity changes, i.e., localizing the temporal velocity changes in the horizontal and depth  
168 domain of the subsurface, from the continuous recordings of ambient noise using high-resolution  
169 waveform inversion technique.

170 A baseline velocity model is necessary for comparing with the time-lapse subsurface models. We  
171 use the full waveform inversion (FWI) (Tarantola, 1984; Shipp & Singh, 2002; Guo et al., 2022)  
172 technique for estimating a high-resolution baseline model using the extracted Scholte waves. For  
173 its numerical implementation, a gradient-based linearized inversion approach is used for  
174 updating the velocity model iteratively in the aim of minimizing the misfit between synthetic and  
175 observed data, with the gradients of the data misfit to model parameters efficiently calculated by  
176 the adjoint-state method from the cross-correlation of the source and adjoint wavefields  
177 (Tarantola, 1984; Fichtner et al., 2006). The source and adjoint wavefields can be obtained by  
178 source-wavelet generated forward wave propagation and adjoint-source generated backward  
179 wave propagation (Shipp & Singh 2002). We use time-domain staggered-grid finite-difference  
180 (Virieux, 1986) with fourth-order spatial and second-order temporal accuracy for solving the  
181 elastic-wave equation in the stress and particle-velocity formulation.

182 We use the baseline data in the form of common-station gathers (e.g., Fig. 3) as the observed  
183 data for the baseline FWI. Considering that the phase information in the virtual Scholte waves of  
184 the CC functions is more reliable than the amplitude, here we use a trace-normalized FWI  
185 method (Shen, 2010) where each seismic trace is normalized by the l-2 norm of the trace itself in  
186 the misfit function (Text S1).

187 Fig. S3a shows the velocity model from the wave-equation dispersion inversion, which uses the  
188 adjoint-state method for fitting the surface wave dispersion spectra (Li et al. 2017; Chen &  
189 Saygin, 2022). With the model in Fig. S3a as the starting model, Fig. 4a shows the velocity  
190 model from the baseline trace-normalized FWI after 50 iterations. The data misfit has been much  
191 reduced after FWI (Fig. S4). The synthetically calculated data after the FWI show much better

192 match (Fig. S5) to the extracted Scholte wave arrivals of the observed baseline data than those  
 193 from the starting model. The velocity model in Fig. 4a is used as the baseline model for  
 194 computing time-lapse seafloor models.



195  
 196 Fig. 4. Baseline velocity model and time-lapse subsurface models of velocity changes in the shallow  
 197 seafloor. (a) The high-resolution baseline velocity model from trace-normalized FWI, which is used as the  
 198 starting model for DD-WI. (b) The time-lapse image of velocity changes for Hour 15 Day 1. (c) The time-  
 199 lapse image of velocity changes for Hour 1 Day 2. The black triangles in (a) indicate the locations of the  
 200 OBNs.

### 201 3.3 Double-difference waveform inversion for localizing time-lapse velocity changes

202 The most straightforward approach for generalizing seismic inversion to the time-lapse monitoring  
 203 is to perform two inversions for the baseline and the monitoring data respectively, however the  
 204 results are sensitive to the baseline model and could be heavily contaminated by the residual data  
 205 misfit from the baseline inversion (Yang et al., 2016). Double-difference waveform inversion (DD-

206 WI (Denli and Huang, 2009) using differential waveforms has been used for providing more  
 207 reliable subsurface models of velocity changes with body waves from controlled sources.

208 The time-lapse difference of the data mainly manifests in the travel times (Fig. 3), which suggests  
 209 that an objective function of the seismic time-lapse inversion problem using travel time differences  
 210 (shifts) between the monitoring and baseline data may be the most stable for quantifying the time-  
 211 lapse velocity models. DD-WI using travel time differences as an objective function has been  
 212 proposed before, but in the background of seismic adjoint tomography for estimating seismic wave  
 213 velocity structures, where the differential measurements are constructed between receivers (Yuan  
 214 et al., 2016). We introduce it for elastic-wave equation based time-lapse inversion where the  
 215 differential measurements are constructed between baseline and monitoring data.

216 Here, we propose the DD-WI method using travel time differences for obtaining time-lapse  
 217 velocity models using the extracted Scholte waves from ambient noise. The misfit function is  
 218 defined as

$$219 \quad J = \sum_{i=1}^{N_s} \sum_{j=1}^{N_r} \|\Delta t_{i,j}^d - \Delta t_{i,j}^s\|^2 \quad (1)$$

220 where  $\Delta t_{i,j}^d$  is the travel time difference between the monitoring and the baseline observed data,  
 221 and  $\Delta t_{i,j}^s$  is the travel time difference between the synthetic data from the monitoring model and  
 222 the baseline FWI model.  $i$  and  $j$  are the indexes for the sources and receivers,  $N_s$  and  $N_r$  are the  
 223 number of sources and receivers. The time difference (shift) can be estimated by comparing  
 224 waveform data using cross correlation. The term ‘double-difference’ comes from the two-level  
 225 differences in equation 3: (1) the difference between baseline and monitoring data, either synthetic  
 226 or observed, and (2) the difference between the synthetic and observed measurements from (1).

227 The adjoint source for the DD-WI of travel time differences (Yuan et al., 2016), which is used for  
 228 elastic wave propagation in backward time steps for computing the adjoint wavefields, can be  
 229 derived as

$$230 \quad \chi_{i,j} = [\Delta t_{i,j}^d - \Delta t_{i,j}^s] \partial_t s_{i,j}(t - \Delta t_{i,j}^s), \quad (2)$$

231 where  $s_{i,j}$  is a seismic waveform trace (1-D time-series vector) from the synthetic data. The only  
232 difference with the FWI is the adjoint source. Both the baseline and time-lapse inversion methods  
233 honor the seafloor bathymetry which is implicitly included when solving the elastic-wave  
234 equation. We apply the DD-WI method to the differential measurements of monitoring and  
235 baseline data for localizing the shear-wave velocity changes in the seafloor at an hourly basis. The  
236 misfit has been largely reduced after inversion (Fig. S6). The derived velocity difference between  
237 the model of Hour 15 Day 1 and the baseline model is shown in Fig. 4b, with that of Hour 1 Day  
238 2 shown in Fig. 4c. The changes in Fig. 4b are overall negative suggesting a slower velocity than  
239 the baseline model, while the velocity differences in Fig. 4c are mainly positive indicating a faster  
240 velocity than the baseline; both are in agreement with Figs. 2 and 3. We also observe that the  
241 velocity changes are more significant at the shallower depths, up to  $\sim 1\%$  relative to the baseline  
242 model, consistent with Fig. 2b where there are larger temporal velocity changes from the CC  
243 functions of smaller offsets (shallower depth) than those of the larger offsets (Fig. 2b). We estimate  
244 time-lapse models of velocity changes from more hours (Figs. S7, S8). We also apply the inversion  
245 method to the monitoring data from more survey lines (Figs. S9, S10); the localized time-lapse  
246 velocity changes of the seafloor show consistent increase/decrease patterns with Fig. S2.

#### 247 **4 Discussion**

248 The observed temporal velocity changes (up to  $\sim 1\%$ ) is subtle, especially when compared with the  
249 likely difference between the baseline model from FWI and the ground truth of the seafloor. It is  
250 important to test if these velocity changes are real, not coming from the unfitted data in the baseline  
251 inversion. Therefore we perform a series of synthetic tests (Text S2, Fig. S11-S16), especially with  
252 errors in the baseline model and noise in the baseline and time-lapse data. The inversion results  
253 suggest that the proposed method is robust to data noise and errors in the baseline model, and the  
254 velocity temporal changes localized by DD-WI using differential travel times are reliable.

255 Surface wave or ambient noise tomography using wave dispersion measurements is usually  
256 performed using a two-step approach, where the construction of 2-D maps of phase/group  
257 velocities at series of frequencies is followed by a point-wise inversion of dispersion data for 1-D  
258 depth profiles at each grid point (Bodin & Sambridge, 2009). This approach assumes smoothly  
259 varying medium and may suffer from lateral discontinuity; furthermore the minor waveform  
260 changes in the monitoring data may be difficult to track from dispersion. On the other hand, we

261 build the baseline shear-wave velocity model from surface waves using wave-equation dispersion  
262 inversion followed by FWI to further improve the accuracy and resolution, and finally DD-WI of  
263 arrival time shifts for time-lapse images. The models are updated based on the adjoint-state method  
264 with a numerical solution of the full elastic-wave equation for arbitrarily complicated medium. In  
265 contrast with the two-step method, the inversions we used are able to provide velocity models in  
266 the horizontal and depth domain from surface waves in one step with a few iterations. The  
267 inversion is sensitive to subtle subsurface property changes by comparing the waveforms directly  
268 using the full physics.

269 In this study we limit the maximum offset to be 3 km. It is straightforward to include CC functions  
270 from larger offsets for monitoring subsurface property change at the greater depths, but likely with  
271 a lower temporal resolution because of longer recording time of ambient noise for the CC function  
272 convergence. Body waves have been observed in the auto- and cross-correlation functions of  
273 seismic ambient noise (Roux et al., 2005; Nakata et al., 2016; Saygin et al., 2017). As we use DD  
274 measurements of arrival times rather than wave dispersion, the proposed method can be applied  
275 for monitoring using body waves (Brenquier et al., 2020). While we apply the method per survey  
276 line, the method is ready for estimating subsurface velocity change models in 3-D (the horizontal  
277 plane and depth) using 3-D elastic-wave equations, provided that the 3-D seismic responses can  
278 be accurately reconstructed from ambient noise. The time-lapse inversion method is easy to  
279 implement with existing FWI source codes by simply changing the adjoint source for backward  
280 wavefield propagation. Time-lapse inversion using DD measurements of arrival times can also be  
281 implemented using ray-tracing, however elastic-wave equation describes the complete wave  
282 phenomena without the high-frequency approximation.

283 The extracted seismic responses contain two parts: the direct (ballistic) waves and the coda part  
284 (Shapiro and Campillo, 2004). We apply the method to the ballistic part of the Scholte waves. The  
285 coda part can be more sensitive to subtle velocity changes because the multiple scattering process  
286 caused by heterogeneities samples the propagation medium very densely and for a long time (Sens-  
287 Schönfelder and Wegler, 2006) and has been widely used for detecting very small velocity changes  
288 with a spatially uniform change assumption (Hillers et al., 2014). However its convergence requires  
289 longer recording time and the sophisticated propagation paths make inversion difficult. Apart from  
290 localizing the velocity changes from ballistic surface wave arrivals (de Ridder et al., 2014; Mordret

291 et al., 2014, 2020), there have been studies for determining the spatial extent of changes from coda  
292 waves using sensitivity kernels (Obermann et al., 2013), which is derived based on the diffusion  
293 approximation (Pacheco & Snieder, 2005) and is more of a modeling perspective. The resolution  
294 is lower than that from the wave-equation based inversion.

295 The observed changes of shear-wave velocity decrease with increasing depths, generally follows  
296 the seafloor bathymetry and seems to have a 24-hour cycling pattern. Previous studies (e.g.,  
297 Takano et al., 2014) have related onshore crustal velocity changes of 0.1-0.3% to the solid earth  
298 tide from the gravitational field of the Sun and Moon, which could cause the opening/closure of  
299 cracks or pores in the shallow subsurface leading to velocity decrease/increase respectively. The  
300 periodicity of non-volcanic tremor at the subduction zone (Nakata et al., 2008) and the  
301 microseismicity at the Mid-Atlantic Ridge (Leptokaropoulos et al., 2021) can also be induced by  
302 the earth tide. The changes in sea height caused by the ocean tide through the influence of gravity  
303 can create overburden loading variations on the seafloor and cause temporal velocity changes  
304 (Dean et al., 1994). The velocity changes caused by earth tide decrease with depths (Hillers et al.,  
305 2015), consistent with what we have observed. In addition to the solid earth and ocean tides, the  
306 pressure loading of long-wavelength ocean infragravity waves can also induce seafloor vertical  
307 deformation (seafloor compliance), which is sensitive to the shear modulus structure (Crawford et  
308 al., 1999) and therefore could cause shear-wave velocity temporal changes. The physical  
309 mechanism behind the sinusoidal temporal velocity changes (up to 1%) in the shallow seafloor  
310 observed at this site remain under investigation.

311

## 312 **5 Conclusions**

313 In this study, we demonstrate that the new passive monitoring technique provides a cost-effective  
314 and environmentally-friendly solution for real-time 4-D quantitative monitoring of subsurface  
315 property changes with high temporal (hourly) and spatial (hundreds of meters) resolution. Using  
316 seismic ambient noise data recorded by a dense array of OBNs offshore Western Australia, we  
317 detect temporal variations of shear-wave velocity up to 1% in the seafloor, with a likely 24-hour  
318 cycling pattern. To localize the velocity changes in the subsurface, we first build a high-  
319 resolution baseline seafloor model from FWI of Scholte waves. Then from DD-WI of wave

320 arrival time differences we obtain the quantitative time-lapse seafloor images containing the  
321 heterogeneous relative velocity variations in the horizontal and depth domain, where the velocity  
322 changes decrease with increasing depths. The elastic-wave equation based workflow from  
323 building high-resolution baseline model to time-lapse inversion using surface wave  
324 measurements honors the full wave physics, is robust to data noise and errors from the baseline  
325 model, and is sensitive to subtle velocity changes, which can be applied to dense passive seismic  
326 data from seismic arrays and Distributed Acoustic Sensing (DAS) for real-time monitoring of  
327 groundwater level, volcano, subduction zone and CO<sub>2</sub> capture storage, in the aim for an in-depth  
328 understanding of the evolving 4-D Earth.

329

### 330 **Acknowledgments**

331 This research was funded by the Deep Earth Imaging Future Science Platform, CSIRO. This  
332 work was supported by resources provided by the Pawsey Supercomputing Centre with funding  
333 from the Australian Government and the Government of Western Australia. The raw seismic  
334 data of the Gorgon Ocean Bottom Node Seismic Survey (ID: ENO0603054) can be requested  
335 from the National Offshore Petroleum Information Management System (NOPIMS) via  
336 contacting [AusGeoData@ga.gov.au](mailto:AusGeoData@ga.gov.au). We thank Chevron Australia for their assistance with the  
337 data. We thank Dr. Yuqing Chen for providing the starting model of shear-wave velocity for  
338 baseline FWI.

339

### 340 **Open Research**

341 The data used for reproducing the figures, including the hourly CC functions,  $dv/v$  measurements  
342 and seismic velocity models, are publicly available at <https://doi.org/10.5281/zenodo.6804990>.

343

### 344 **References**

- 345 Bodin, T., & Sambridge, M. (2009). Seismic tomography with the reversible jump algorithm.  
346 *Geophysical Journal International*, 178(3), 1411-1436.
- 347 Brenguier, F., Shapiro, N. M., Campillo, M., Ferrazzini, V., Duputel, Z., Coutant, O., & Nercessian, A.  
348 (2008). Towards forecasting volcanic eruptions using seismic noise. *Nature Geoscience*, 1(2), 126-130.

- 349 Brenguier, F., Rivet, D., Obermann, A., Nakata, N., Boué, P., Lecocq, T., ... & Shapiro, N. (2016). 4-D  
350 noise-based seismology at volcanoes: Ongoing efforts and perspectives. *Journal of Volcanology and*  
351 *Geothermal Research*, 321, 182-195.
- 352 Brenguier, F., Courbis, R., Mordret, A., Campman, X., Boué, P., Chmiel, M., ... & Hollis, D. (2020).  
353 Noise-based ballistic wave passive seismic monitoring. Part 1: body waves. *Geophysical Journal*  
354 *International*, 221(1), 683-691.
- 355 Chen, Y. and Saygin, E. (2022). 3-D S Wave Imaging via Robust Neural Network Interpolation of 2-D  
356 Profiles from Wave equation Dispersion Inversion of Seismic, *J. Geophys. Res.-Solid Earth*, in-review.  
357 <https://www.essoar.org/doi/abs/10.1002/essoar.10511223.1>
- 358 Crawford, W. C., Webb, S. C., & Hildebrand, J. A. (1999). Constraints on melt in the lower crust and  
359 Moho at the East Pacific Rise, 9 48' N, using seafloor compliance measurements. *Journal of Geophysical*  
360 *Research: Solid Earth*, 104(B2), 2923-2939.
- 361 Dean, G., Hardy, R., & Eltvik, P. (1994). Monitoring compaction and compressibility changes in offshore  
362 chalk reservoirs. *SPE Formation Evaluation*, 9(01), 73-76.
- 363 Denli, H., & Huang, L. (2009). Double-difference elastic waveform tomography in the time domain. In  
364 *SEG Technical Program Expanded Abstracts 2009* (pp. 2302-2306). Society of Exploration  
365 Geophysicists.
- 366 De Ridder, S. A. L., & Biondi, B. L. (2013). Daily reservoir-scale subsurface monitoring using ambient  
367 seismic noise. *Geophysical Research Letters*, 40(12), 2969-2974.
- 368 De Ridder, S. A. L., Biondi, B. L., & Clapp, R. G. (2014). Time-lapse seismic noise correlation tomography  
369 at Valhall. *Geophysical Research Letters*, 41(17), 6116-6122.
- 370 Fichtner, A., Bunge, H. P., & Igel, H. (2006). The adjoint method in seismology: I. Theory. *Physics of the*  
371 *Earth and Planetary Interiors*, 157(1-2), 86-104.
- 372 Guo, P., Singh, S.C., Vaddineni, V.A. et al. (2022). Lower oceanic crust formed by in situ melt  
373 crystallization revealed by seismic layering. *Nature Geoscience*, [https://doi.org/10.1038/s41561-022-](https://doi.org/10.1038/s41561-022-00963-w)  
374 [00963-w](https://doi.org/10.1038/s41561-022-00963-w)
- 375 Hicks, E., Hoeber, H., Houbiers, M., Lescoffit, S. P., Ratcliffe, A., & Vinje, V. (2016). Time-lapse full-  
376 waveform inversion as a reservoir-monitoring tool—A North Sea case study. *The Leading Edge*, 35(10),  
377 850-858.
- 378 Hillers, G., Retailleau, L., Campillo, M., Inbal, A., Ampuero, J. P., & Nishimura, T. (2015). In situ  
379 observations of velocity changes in response to tidal deformation from analysis of the high-frequency  
380 ambient wavefield. *Journal of Geophysical Research: Solid Earth*, 120(1), 210-225.
- 381 Kamei, R. and D. Lumley (2017). Full waveform inversion of repeating seismic events to estimate time-  
382 lapse velocity changes. *Geophysical Journal International* 209(2), 1239–1264.

- 383 Leptokaropoulos, K., Harmon, N., Hicks, S. P., Rychert, C. A., Schlaphorst, D., & Kendall, J. M. (2021).  
384 Tidal triggering of microseismicity at the Equatorial Mid-Atlantic Ridge, Inferred from the PI-LAB  
385 experiment. *Journal of Geophysical Research: Solid Earth*, 126(9), e2021JB022251.
- 386 Li, J., Feng, Z., & Schuster, G. (2017). Wave-equation dispersion inversion. *Geophysical Journal*  
387 *International*, 208(3), 1567-1578.
- 388 Lumley, D. E. (2001). Time-lapse seismic reservoir monitoring. *Geophysics*, 66(1), 50-53.
- 389 Mao, S., M. Campillo, R. D. van der Hilst, et al. (2019). High temporal resolution monitoring of small  
390 variations in crustal strain by dense seismic arrays. *Geophysical Research Letters* 46(1), 128–137.
- 391 Mordret, A., Courbis, R., Brenguier, F., Chmiel, M., Garambois, S., Mao, S., ... & Hollis, D. (2020).  
392 Noise-based ballistic wave passive seismic monitoring–Part 2: surface waves. *Geophysical Journal*  
393 *International*, 221(1), 692-705.
- 394 Mordret, A., N. M. Shapiro, and S. Singh (2014). Seismic noise-based time-lapse monitoring of the  
395 valhall overburden. *Geophysical Research Letters* 41(14), 4945–4952.
- 396 Nakata, N., Boué, P., Brenguier, F., Roux, P., Ferrazzini, V., & Campillo, M. (2016). Body and surface  
397 wave reconstruction from seismic noise correlations between arrays at Piton de la Fournaise volcano.  
398 *Geophysical Research Letters*, 43(3), 1047-1054.
- 399 Nakata, R., Suda, N., & Tsuruoka, H. (2008). Non-volcanic tremor resulting from the combined effect of  
400 Earth tides and slow slip events. *Nature Geoscience*, 1(10), 676-678.
- 401 Obermann, A., Planès, T., Larose, E., Sens-Schönfelder, C., & Campillo, M. (2013). Depth sensitivity of  
402 seismic coda waves to velocity perturbations in an elastic heterogeneous medium. *Geophysical Journal*  
403 *International*, 194(1), 372-382.
- 404 Pacheco, C., & Snieder, R. (2005). Time-lapse travel time change of multiply scattered acoustic waves.  
405 *The Journal of the Acoustical Society of America*, 118(3), 1300-1310.
- 406 Richter, T., Sens-Schönfelder, C., Kind, R., & Asch, G. (2014). Comprehensive observation and  
407 modeling of earthquake and temperature-related seismic velocity changes in northern Chile with passive  
408 image interferometry. *Journal of Geophysical Research: Solid Earth*, 119(6), 4747-4765.
- 409 Roche, B., Bull, J. M., Marin-Moreno, H., Leighton, T. G., Falcon-Suarez, I. H., Tholen, M., ... &  
410 Faggetter, M. (2021). Time-lapse imaging of CO<sub>2</sub> migration within near-surface sediments during a  
411 controlled sub-seabed release experiment. *International Journal of Greenhouse Gas Control*, 109, 103363.
- 412 Rodríguez Tribaldos, V., & Ajo-Franklin, J. B. (2021). Aquifer monitoring using ambient seismic noise  
413 recorded with distributed acoustic sensing (DAS) deployed on dark fiber. *Journal of Geophysical*  
414 *Research: Solid Earth*, 126(4), e2020JB021004.
- 415 Roux, P., Sabra, K. G., Gerstoft, P., Kuperman, W. A., & Fehler, M. C. (2005). P-waves from cross-  
416 correlation of seismic noise. *Geophysical Research Letters*, 32(19).

- 417 Saygin, E., Cummins, P. R., & Lumley, D. (2017). Retrieval of the P wave reflectivity response from  
418 autocorrelation of seismic noise: Jakarta Basin, Indonesia. *Geophysical Research Letters*, 44(2), 792-799.
- 419 Schimmel, M., Stutzmann, E., & Gallart, J. (2011). Using instantaneous phase coherence for signal  
420 extraction from ambient noise data at a local to a global scale. *Geophysical Journal International*, 184(1),  
421 494-506.
- 422 Sens-Schönfelder, C. and U. Wegler (2006). Passive image interferometry and seasonal variations of  
423 seismic velocities at Merapi volcano, Indonesia. *Geophysical Research Letters* 33 (21), L21302.
- 424 Shapiro, N. M. and M. Campillo (2004). Emergence of broadband rayleigh waves from correlations of the  
425 ambient seismic noise. *Geophysical Research Letters* 31(7).
- 426 Shen, X. (2010). Near-surface velocity estimation by weighted early-arrival waveform inversion. In SEG  
427 Technical Program Expanded Abstracts 2010 (pp. 1975-1979). Society of Exploration Geophysicists.
- 428 Shipp, R. M., & Singh, S. C. (2002). Two-dimensional full wavefield inversion of wide-aperture marine  
429 seismic streamer data. *Geophysical Journal International*, 151(2), 325-344.
- 430 Stehly, L., Campillo, M., & Shapiro, N. M. (2006). A study of the seismic noise from its long-range  
431 correlation properties. *Journal of Geophysical Research: Solid Earth*, 111(B10).
- 432 Takano, T., Brenguier, F., Campillo, M., Peltier, A., & Nishimura, T. (2020). Noise-based passive ballistic  
433 wave seismic monitoring on an active volcano. *Geophysical Journal International*, 220(1), 501-507.
- 434 Takano, T., Nishimura, T., Nakahara, H., Ohta, Y., & Tanaka, S. (2014). Seismic velocity changes caused  
435 by the Earth tide: Ambient noise correlation analyses of small-array data. *Geophysical Research Letters*,  
436 41(17), 6131-6136.
- 437 Tarantola, A. (1984). Inversion of seismic reflection data in the acoustic approximation. *Geophysics*. 49,  
438 1259-1266.
- 439 Virieux, J. (1986). P-SV wave propagation in heterogeneous media: Velocity-stress finite-difference  
440 method. *Geophysics*, 51(4), 889-901.
- 441 Yang, D., Liu, F., Morton, S., Malcolm, A., & Fehler, M. (2016). Time-lapse full-waveform inversion with  
442 ocean-bottom-cable data: Application on Valhall field. *Geophysics*, 81(4), R225-R235.
- 443 Yuan, Y. O., Simons, F. J., & Tromp, J. (2016). Double-difference adjoint seismic tomography.  
444 *Geophysical Journal International*, 206(3), 1599-1618.
- 445 Zhang, Z., & Huang, L. (2013). Double-difference elastic-waveform inversion with prior information for  
446 time-lapse monitoring. *Geophysics*, 78(6), R259-R273.

447

448

449